Article

High-Throughput Synthesis and Screening of Iridium(III) Photocatalysts for the Fast and Chemoselective Dehalogenation of Aryl Bromides

Velabo Mdluli, Stephen DiLuzio, Jacqueline Lewis, Jakub Kowalewski,
Timothy U. Connell, David Yaron, Tomasz Kowalewski, and Stefan Bernhard

Just Accepted

High-Throughput Synthesis and Screening of Iridium(III) Photocatalysts for the Fast and Chemoselective Dehalogenation of Aryl Bromides

Velabo Mdluli, Stephen Diluzio, Jacqueline Lewis, Jakub F. Kowalewski, Timothy U. Connell, David Yaron, Tomasz Kowalewski, Stefan Bernhard*

Department of Chemistry, Carnegie Mellon University, Pittsburgh, Pennsylvania 15213, USA

ABSTRACT

A high-throughput optical screening method for the photocatalytic activity of a structurally diverse library of 1152 cationic iridium(III) complexes ($[Ir(C^\wedge N)_2(N^\wedge N)]^+$), corresponding to all combinations of 48 cyclometalating ($C^\wedge N$) and 24 ancillary ($N^\wedge N$) ligands, was developed. This rapid assay utilizes the colorimetric changes of a high contrast indicator dye, coumarin 6, to monitor the photo-induced electron transfer from a sacrificial amine donor to the metal complex excited state. The resulting $[Ir(C^\wedge N)_2(N^\wedge N)]^0$ can then reduce an aryl bromide to form the highly reactive aryl radical intermediate. The rate of this reaction is dictated by the molecular structure of both coordinating ligands. Relative reaction rate constants determined *via* this method correlated closely with ^{19}F NMR measurements obtained using a fluorinated substrate. A simple model that expresses the rate constant as a product of a single "strength" parameter assigned to each of the 72 ligands can well account for the 1152 measured rate constants. The best performing complexes exhibit much higher reactivity than the benchmark photocatalysts commonly used in photoredox transformations. The catalysts were also successfully tested for their chemoselectivity. The developed screening methodology can enable generation of the large data sets needed to use modern data science to extract structure-activity relationships.

INTRODUCTION

The absorption and conversion of visible light into chemical energy is an enviromentally sustainable and powerful tool in organic synthesis that provides access to reactive, open-shell intermediates under mild conditions. Commonly employed pathways to such reactive intermediates include the use of harsh conditions, such as either strong acids or bases, toxic initiators, or high-energy ultraviolet illumination of precursors, that may lead to unwanted side reactions.[1] In contrast, photoredox catalysis exploits the increased oxidative and reductive power of an excited, molecular photocatalyst to promote directed, light-driven electron transfers as a pathway to generate such high-energy, highly reactive species. This attractive strategy, rendered even more powerful when operating in concert with two-electron transition metal catalysts, has driven the rapid expansion of this field over the last decade.[2-4] Photoredox methodology has also been embraced by the chemical manufacturing industry, particularly in the preparation of high-value chemicals including pharmaceuticals and agrochemicals, due to its unparalleled capacity for chemoselective late-stage functionalization.[5-7]

Despite increasing reports that utilize organic dyes and first row transition metal complexes,[8-9] the most widely used catalysts are still coordination complexes of d^6 transition metals, specifically ruthenium(II) and iridium(III). The strong ligating power of cyclometalating ligands and the observed photo and redox stability of the resulting iridium(III) complexes is a highly valuable asset in organic photochemical transformations. It is noteworthy that the unique photophysical properties of heteroleptic iridium(III) complexes of the type $[Ir(C^\wedge N)_2(N^\wedge N)]^+$, where $C^\wedge N$ is a cyclometalating and $N^\wedge N$ is an ancillary 1,2-diimine ligand, are attractive in a wide range of applications in addition to photoredox catalysis, including: water reduction,[10-12] biological imaging[13-15]and optoelectronic devices.[16-18] Irradiation of these complexes generates a long-lived

triplet excited state, facilitated by the large spin-orbit coupling constant of the heavy metal atom. Spatially partitioned frontier orbitals also allow for judicious tuning of redox and optical properties; the highest occupied molecular orbital (HOMO) centers on the C^N ligand while the lowest unoccupied molecular orbital (LUMO) is located on the N^N ligand. Independent control of these orbitals (Figure 1) should allow a 'push-pull' design approach to tune the HOMO-LUMO gap and redox potentials, enabling careful selection of a photocatalyst that matches the energy demands of a specific chemical substrate or process. It is therefore surprising that the vast scope of synthetic photoredox methodology is derived from a limited number of complexes, centered around the commercially available, cationic $[Ir(ppy)_2(dtbbpy)]^+$ and $[Ir(dF(CF_3)ppy)_2(dtbbpy)]^+$ complexes.

Optimal catalyst selection can be accelerated by high-throughput synthesis and screening (HTSS) techniques. Cost-efficient screening of multiple reactions using conventional analytical methods is both difficult and time consuming, but colorimetric reagents provide a simple, yet robust optical response that has been successfully applied in electrocatalysis,[19-21] organic synthesis,[22-26] olefin polymerization[27] and the preparation of solid state materials.[28] Online monitoring of parallelized reactions provides even greater value by revealing chemical reaction kinetics under standardized conditions.[29-32] Finally, HTSS generates large amounts of data that enables the growing field of data-driven science, described as the fourth approach to chemical discovery, in addition to experimentation, theory and computation.[33] Such methodology requires the pioneering development of more revealing data visualization techniques and powerful statistical approaches in the chemical sciences; the use of machine learning algorithms is one example of such a thrust that was employed to better understand structure-reactivity relationships in catalytic systems.[34-37]

In this work, we report an innovative methodology that allowed for HTSS of a structurally diverse library of 1152 distinct [Ir(C^N)$_2$(N^N)]$^+$ photocatalysts (the explored C^N and N^N structures are shown in the Supporting Information). This was achieved by monitoring the drastic quenching of an indicator dye's luminescence by protons generated during a model photochemical reaction. Several of the complexes were subsequently prepared in batch *via* conventional methodologies and compared to two iridium(III) photocatalysts, [Ir(ppy)$_2$(dtbbpy)]PF$_6$ and [Ir(dF(CF$_3$)ppy)$_2$(dtbbpy)]PF$_6$, commonly used in photoredox synthesis. Not only did some of the newly discovered Ir(III) chromophores exhibit faster reaction kinetics, but also presented choices for pursuing chemoselective photochemical reactions.
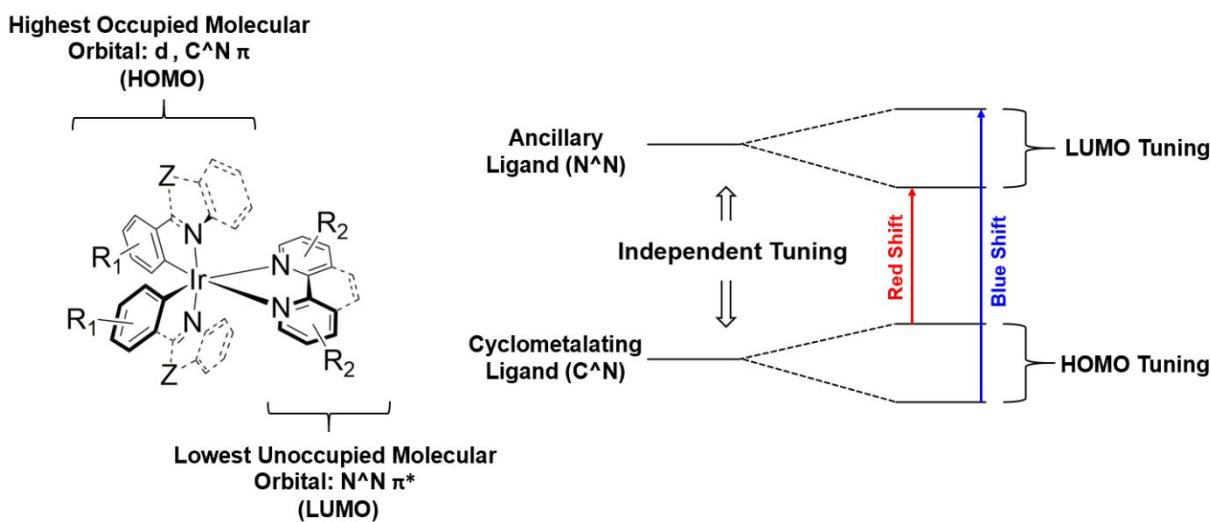
**Figure. 1**. The frontier orbitals (highest and lowest occupied molecular orbitals) are well-partitioned in [Ir(C^N)$_2$(N^N)]$^+$ photocatalysts, enabling the judicious tuning of photophysical and redox properties *via* structural modification of the cyclometalating (C^N) and ancillary (N^N) ligands.

EXPERIMENTAL METHODS

General Considerations

All reagents and solvents were commercially sourced and used without further purification, unless otherwise stated. Nuclear magnetic resonance (NMR) spectra were obtained using Bruker Avance and NOE 500 MHz spectrometers; ^{1}H and ^{13}C spectra were referenced to residual solvent peaks, ^{19}F NMR used the PF_6 anion signal (δ -71.11 ppm) as an internal standard. Electrospray ionization mass spectrometry (ESI-MS) was performed on a Thermo-Fisher LCQ instrument. Synthesis of cyclometalating ligands (C^N) and iridium(III) dimers followed previously published procedures.[38-42]

Photoreactor Design

SOLIDWORKS design files and Python control software for custom-built photoreactors are supplied in the Supporting Information. High intensity illumination (Chanzon 100 W Royal Blue LEDs) of a 96-well plate equipped with 1 mL shell vials containing iridium(III) luminophores was monitored with a AuviPal 5 Megapixel Raspberry Pi Camera (Module 1080p OV5647 Sensor) mounted between the light sources (Figure 2). Reactions were run under an inert argon atmosphere, maintained at positive pressure and monitored using a Winsen ME2-O_2-Φ20 oxygen sensor. Top-down illumination for photography utilized six pairs of colored Chanzon 10 W LEDs: warm white (3000K-3500K), ultraviolet (375nm), blue (440-450nm), green (520-525 nm), yellow (590-592 nm) and red (650-660nm). The lighting was controlled with a Raspberry Pi computer through an eight-channel relay board that also controlled the USB camera.
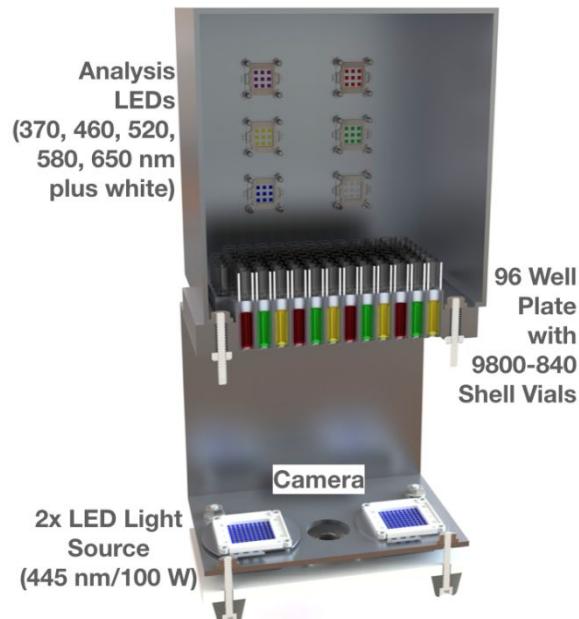
Figure 2: Rendering of a SOLIDWORKS design plan for the custom-built 96-well photoreactor that was used for monitoring the reaction progress of reductive debromination reactions. Two 100W blue LED light sources illuminate shell vials through the bottom. Reaction progress is monitored by camera using six 10W LEDs of various colors to illuminate samples from above.

Colorimetric Screening

Solutions of $[Ir(C^{\wedge}N)_2Cl]_2$ dimers (100 µL, 0.3 mM) and $N^{\wedge}N$ ancillary ligand (100 µL, 0.6 mM) in dimethylsulfoxide were pippetted into 1 mL 9800-840 glass shell vials across twelve columns and eight rows of a 96-well plate, respectively. The sealed solutions were heated at 150 ᵒC overnight to produce heteroleptic iridium(III) complexes ($[Ir(C^{\wedge}N)_2(N^{\wedge}N)]^+$) as previously reported.[39] The cleavage of $[Ir(C^{\wedge}N)_2Cl]_2$ dimers by diimine ligands to form catinic irdium (III) complexes proceeds with ease and high efficiency. Once cooled, 400 µL of a dimethylformamide solution containing varied amounts of aryl bromide, sacrificial electron donor and coumarin 6 was added to each vial. The resulting solution was mixed throughly by resealing and shaking the plate

for several minutes. The vials were transferred to the reactor and degassed under argon for two hours. When the oxygen sensor readings reached zero, vials were irradiated with high intensity blue LEDs for two minutes, followed by image capture under the 10 W LED lights. This irradiation/imaging cycle repeated continuously for five hours. Representative images of the synthesis, reactor set-up and raw experimental pictures are included in the Supporting Information. Compiled photos were analyzed using a custom-written Wolfram Mathematica algorithm that quantifies the changes of the individual reaction well in a designated color space.

Computational Methods

The electronic structures of iridium(III) complexes were calculated *via* density functional theory (DFT), through geometry optimizations with B3LYP functional and LANL2DZ basis set on Gaussian 09. Analysis of photocatalyst reaction rate constants was done with Python SciKit-learn package.[43]

Phosphorescence Lifetime and Emission Screening

Luminophores were irradiated with a pulsed 365 nm LED, powered by a 40 ns square pulse from a Siglent SDG1052 function generator. Emission was detected with a Hamamatsu H7732-11 photomultiplier tube connected to a Tektronix TDS3032B digital oscilloscope interfaced to a Raspberry Pi 3 Model B+ computer. Scattered light from the excitation source was removed from acquired spectra using a plexiglass filter (365 nm long pass). Emission spectra were measured concurrently using a StellarNet BLACK-Comet concave grating spectrometer .

Electrochemical Screening

Cyclic voltammetry was performed with a CH-Instrument Electrochemical Analyzer 600C potentiostat. Measurements were conducted in a three-electrode system consisting of silver wire

pseudo-reference electrode, a platinum coil counter electrode, and a glassy carbon working electrode. Solutions (1 mM analyte and 0.1 M tetra-*n*-butylammonium hexafluorophosphate supporting electrolyte) in acetonitrile were degassed and measured under argon. Voltammograms were collected under positive scan polarity with a scan rate of 0.1 V s^{-1} and redox potentials reported relative to a ferrocene internal standard (E^0(Fc$^+$/Fc) = 0.40 V vs SCE).[44]

RESULTS AND DISCUSSION

Method Development

We selected the reductive dehalogenation of aryl halide[45-47] as a robust model for screening the photocatalytic reactivity of iridium(III) photocatalysts. Following irradiation, the excited state photocatalyst is quenched by a sacrificial electron donor (commonly a tertiary amine), liberating a proton from the oxidized amine. An electron is subsequently transferred from the reduced photocatalyst to an electron acceptor (i.e. aryl halide), affording catalyst turnover. The reactive aryl radical generated can participate in a range of C–C and C–X coupling pathways,[48] however without a suitable nucleophile or electrophile, the radical abstracts a hydrogen atom from the solvent system affording the dehalogenated product (Scheme 1).

Scheme 1. The photoredox reaction being monitored *via* colorimetric changes of coumarin 6 indicator dye.
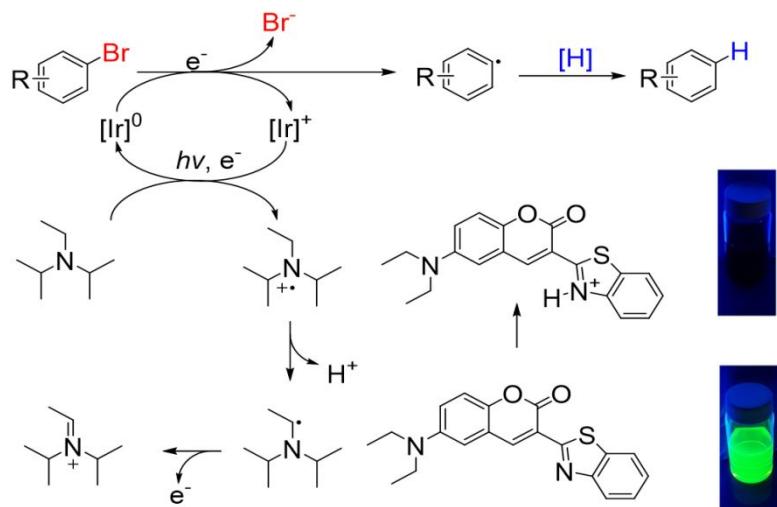
Using a fluorinated aryl bromide reagent allows the reaction to be monitored *via* ^{19}F NMR, showing an exponential decay in the amount of starting material and a corresponding increase in

the amount of product (see Supporting Information). Because the studied reactions are complete within a couple of hours, monitoring the reaction progress on a 96-well plate with ^{19}F NMR is unattainable. To compare the rates of different photocatalysts, a faster, more efficient and low-cost online screening method that uses an appropriate indicator dye was sought. Bromocresol green is an acid sensitive, colorimetric reagent previously used in post-reaction titration to determine the effectiveness of aryl halide reduction.[49] Unfortunately, it is also susceptible to debromination under photoredox conditions and therefore unsuitable for a time-based assay. Instead we selected coumarin 6 (Scheme 1), which exhibits an intense absorption band (λ_{abs} = 444 nm, ε = 54 000 M^{-1}cm^{-1}) and high fluorescent quantum yield (λ_{em} = 510–560 nm, Φ = 0.78) that is drastically quenched in the presence of protons.[50-52] Such a definitive record of the sharp colorimetric change provides a diagnostic handle that allows accurate comparison of photoinduced electron transfer rates among the hundreds of photocatalysts being screened.

The suitability of coumarin 6 as an indicator for comparing photoredox reaction rates was evaluated using twelve heteroleptic iridium(III) complexes as photocatalysts for the dehalogenation of 2'-bromo-4'-flouroacetophenone, with *N,N*-diisopropylethylamine (DIPEA) serving as a sacrificial reductant (Figure 3). The *in-situ* prepared photocatalysts all contained the ancillary ligand 4,4′-di-*tert*-butyl-2,2′-bipyridine (**NN6**) with representative cyclometalating ligands selected from a larger combinatorial library employed in our laboratory. The concentration of coumarin 6 varied down each photocatalyst column (0–1.4 mM in 0.2 mM increments).
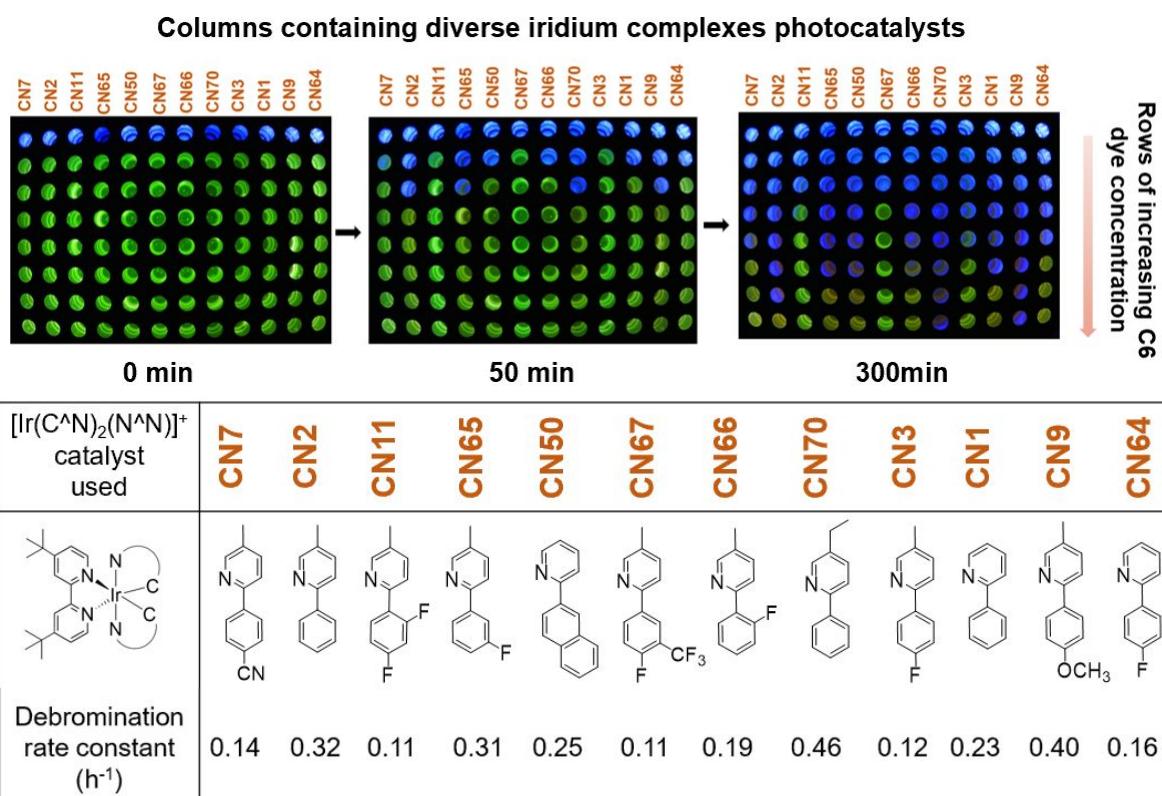
Figure 3. Images of a 96-well plate showing the colorimetric changes of the indicator dye in parallelized photoredox reactions of 12 distinct iridium(III) photocatalysts. Each vial in a column contained 4mM 2'-bromo-4'-flouroacetophenone, 40 mM DIPEA, 0.1 mM photocatalyst and coumarin 6 (C6) indicator dye in increasing concentration down the plate. A video of the reaction progress can be found in the Supporting Information.

Under blue illumination, the neutral dye produces bright green luminescence that is easily observed during imaging. Reaction progress is monitored when this luminescence is quenched by the produced protons, with a drastic colorimetric change observed when no neutral coumarin 6 remains; instead only the blue illumination light is transmitted through a reaction well and detected by the camera. The time required for the sufficient release of protons to reach the equivalence point increases along with increasing amounts of dye through the column. Since the eight reaction wells of each column contain the same photocatalyst, the elementary rate law describing proton

11

production can be deduced; an exponential decay function fitted for each column (see Supporting

Information) revealed that the formation of protons, caused by catalyst-mediated photoinduced

electron transfer, followed first order kinetics.

Rate constants determined *via* HTSS were corroborated by integration of the reactant and

product signals obtained through ^{19}F NMR spectroscopy (Figure 4). The strong linear correlation

($R^2 = 0.98$) of these two techniques confirms the validity of the developed system for comparing

the relative photocatalytic activity of iridium(III) complexes.
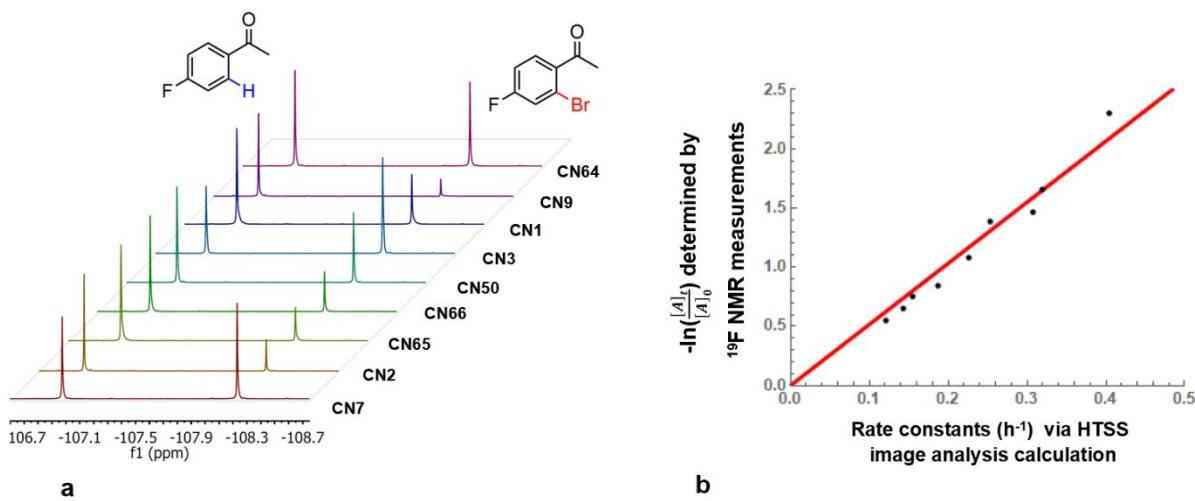
Figure 4. a. Stacked ^{19}F NMR indicating the terminal amounts of reagent (2'-bromo-4'-

flouroacetophenone) and product (4'-fluoroacetophenone) measured via ^{19}F NMR spectroscopy

from the wells of a row on the reaction plate catalyzed by different photocatalysts (Figure 3). **b.**

The ratio $\ln([A]_t/[A]_0)$, where $[A]_t/[A]_0$ is the fraction reactant remaining, measured by NMR, is

linearly correlated to the rate constant obtained *via* image-based analysis of the colorimetric

technique.

Using the developed colorimetric technique, we set out to determine the relative catalytic

activity of 1152 distinct $[Ir(C^{\wedge}N)_2(N^{\wedge}N)]^+$ photocatalysts, comprising 48 C^N and 24 N^N ligands

(structures shown in Supporting Information). For this set, reduction of

12

bromopentafluorobenzene, with its accessible reduction potential,[53] ensured that the results maximized information about relative activity of photocatalysts, rather than being limited by insufficient potential to transfer electrons to a challenging substrate. The reaction conditions (4 mM aryl halide, 40 mM DIPEA, 0.4 mM coumarin 6 and 0.1 mM $[Ir(C^\wedge N)_2(N^\wedge N)]^+$) allowed the calculation of rate constants from the time required to reach an equivalence point representative of 30% substrate reduction.

Prior to the screening of all the hundreds of photocatalysts, a second type of calibration was used to confirm that colorimetric response of the indicator occurs uniformly across the 96-well plate (see video in Supporting Information). This was evaluated by reacting uniform plates with the wells consisting of 96-identical reactions across the entire plate (4mM bromopentafluorobenzene, 40 mM DIPEA, 0.4 mM coumarin 6 and 0.1 mM $[Ir(C^\wedge N)_2(N^\wedge N)]^+$). The PF_6 salts of five traditionally synthesized and isolated Ir (III) complexes were selected for five uniform plates that were expected to exhibit a range of rates constants. Analysis of the plate revealed well-to-well variation of 6 – 14%, in the red-green-blue (RGB) color space, for the all plates. This relative standard deviation within the wells of the five plates was reduced to 4 – 11% when targeted analysis was done along the blue channel of RGB, since the indicator dye detection point is a visible appearance of a blue color. Ultimately, using the Internationale de l'eclairage La*b* (CIELab) which decouples the chromatic part of color from its brightness, resulted in the error range being minimized further still to 2 – 8%. The rate constants for the five uniform plates was calculated to be 0.0 ± 0.0, 0.3 ± 0.02 , 0.8 ± 0.06, 1.5 ± 0.12 and 2.2 ± 0.16 h$^-$^{1} for **$[Ir(CN46)_2(NN6)]^+$, $[Ir(CN11)_2(NN6)]^+$**, **$[Ir(CN1)_2(NN6)]^+$** , **$[Ir(CN70)_2(NN6)]^+$** and **$[Ir(CN34)_2(NN6)]^+$**, respectively. With uniformity across the 96-well plate established, we screened the relative catalytic activity of the 1152 $[Ir(C^\wedge N)_2(N^\wedge N)]^+$ photocatalysts, in the

reduction of bromopentafluorobenzene; all image analysis for this work was done within the

CIELab color space. Figure 5 confirms that the rate constants of the five traditionally synthesized

$[Ir(C^N)_2(N^N)]PF_6$ complexes meausred in these uniform plates and the results obtained with *in-situ* synthesized photocatalysts used for the HTSS (see Supporting Information, attached csv file, for all the rate constants) are within the margins of error.
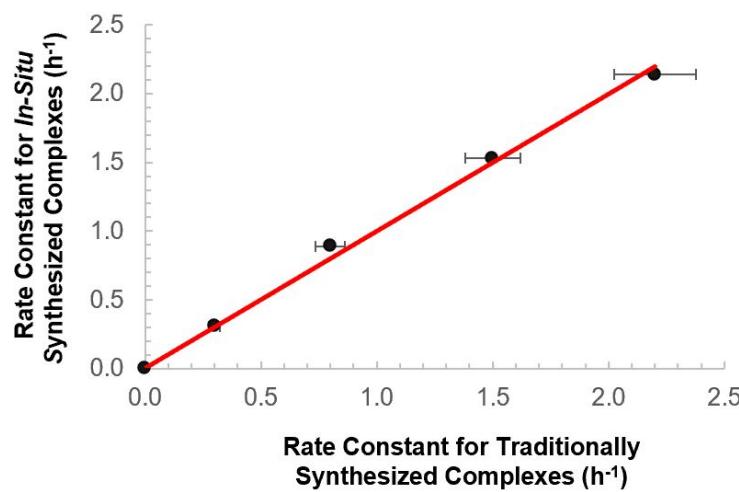
Figure 5. Comparison of the catalytic activity of $[Ir(C^N)_2(N^N)]^+$ complexes utilizing traditionally and *in-situ* synthesized photocatalysts under identical dehalogenation conditions.

Measuring Structure-Activity Relationships

The HTSS rate constants of the 1152 [Ir(C^N)$_2$N^N]$^+$ complexes used in the photo-driven dehalogenationation of bromopentafluorobenzene are attached in Supporting Information. Unlike most studies that synthesize and evaluate a small number of chemically related metal complexes, this large, standardized data set provides a unique opportunity to generalize structure-activity relationships in [Ir(C^N)$_2$N^N]$^+$ photocatalysts. Figure 6 was constructed using a select, but representative, group of C^N and N^N ligands to show some of the major trends.
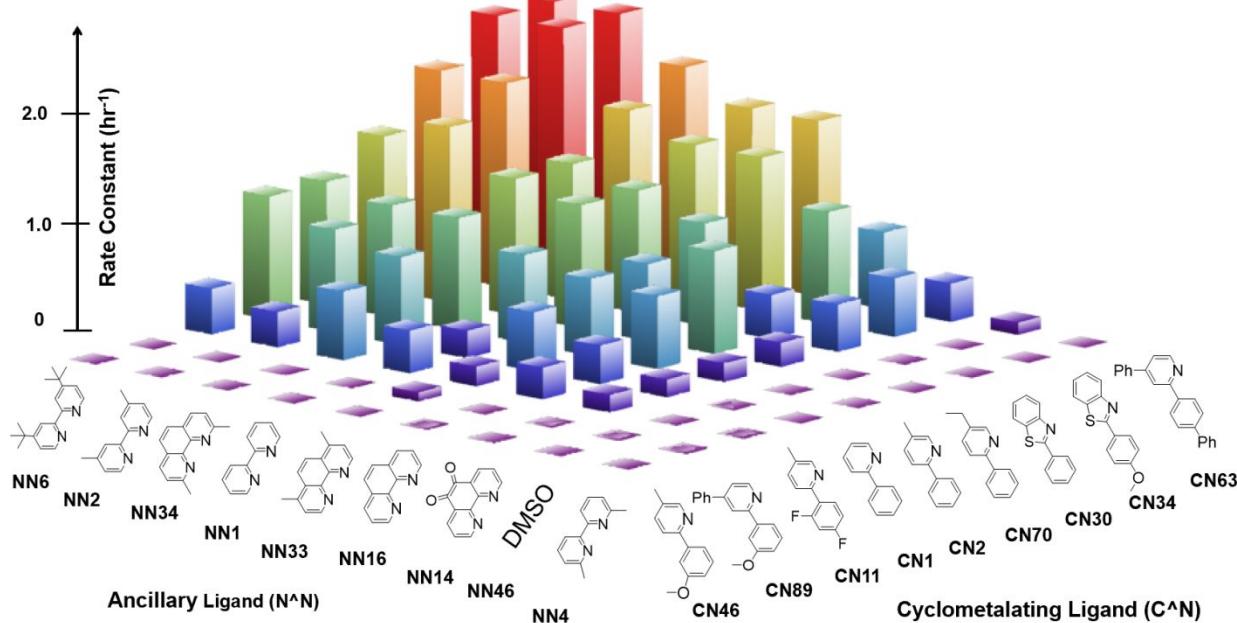
Figure 6. A 3D bar chart, sorted by increasing average rate constants, for a representative set cyclometalating (C^N) and ancillary ligands (N^N) ligands, highlighting some of the major trends of the [Ir(C^N)$_2$N^N]$^+$ photocatalysts. See Supporting Information for array plot.

Alkylation, especially on the pyridyl moiety of the C^N ligand, significantly increased the rate constant of the resulting photocatalyst by donating electron density, as reported in literature.[54] Consider starting with **CN1**, adding a methyl group at the 4- position to the pyridyl ring improves

the resulting photocatalyst (**CN2**), by an average 15% increase in the calculated rate constants. It was quite interesting to discover that using an ethyl substituent (**CN70**) resulted in noticeably greater (35%) enhancement compared to the methyl substitution. Since the electronic structure of the metal complex will not be significantly altered by a change from a methyl to an ethyl substituent, it is likely that the increased steric bulk prevents a N^N ligand dissociation, a known degradation pathway in these photocatalysts.[55] Similarly, the large conjugated systems in 2-phenylbenzothiazole ligands (**CN30** and **CN34**) result in photocatalysts with relatively higher reactivity compared to their 2-phenylpyridine counterparts (**CN30** is nearly two-fold faster than **CN1**). The extent of π conjugation in the C^N ligand is known to drastically impact the nature of the excited state of iridium(III) complex, transforming it to a predominately ^{3}LC excited state.[56-58]

Certain substitutions on the C^N ligand seem to be detrimental to resulting photocatalyst activity, such as electron withdrawing groups (**CN11**), and methoxy groups at the 5-position of the phenyl ring (**CN46** and **CN89**). The diminished ability observed for highly fluorinated photocatalysts can be partly rationalized by considering photocatalyst redox properties: **[Ir(CN1)$_2$NN6]$^+$/[Ir(CN1)$_2$NN6]^0** (E^0 = -1.51 V) is a stronger reductant than its fluorinated cousin, **[Ir(CN11)$_2$NN6]$^+$/[Ir(CN11)$_2$NN6]^0** (E^0 = -1.44 V). This implies that electron transfer from the latter to the aryl halide acceptor is slower, assuming it does not fall into the Marcus-inverted region.[59] With methoxy substituents, para- substituted cyclometalating ligands (**CN34**) exhibit the well understood activation of the resulting photocatalyst, while meta-substitution (**CN46** and **CN89**) produced strongly deactivated photocatalysts; this trend with m-methoxy substituents was also observed when related complexes were employed in light emitting electrochemical cells.[60]

For the ancillary ligands (N^N), the solvated complexes of dimethyl sulfoxide[61] provided

a negative control, and exhibited rate constants close to zero for all tested C^N derivatives. With

the diimines, the data reveals that most bipyridine derivatives outperform those of phenanthroline.

Alkylation of the N^N ligands typically enhanced photocatalyst activity, but for methyl groups at

α-position to the nitrogen donor atoms of an N^N ligand, alkylation is beneficial to the

phenanthroline-based (**NN34**) while being detrimental to the bipyridine ones (**NN4**).   Another

characteristic effect observed with N^N was that the presence of ketone functional groups, e.g.

9,10-phenanthrenedione (**NN14**) significantly reduces photocatalyst activity, likely due to a

dramatic decrease in the HOMO-LUMO gap and the absence of a long-lived excited state.

Data Modeling

The HTSS measured the rate constants for 1152 catalysts consisting of all pairings of 48

cyclometalating (C^N) and 24 ancillary (N^N) ligands. We will denote these experimental rates

as Rate(cn,nn), where cn and nn span the ranges 1 to 48 and 1 to 24, respectively. A striking aspect

of the observed reaction rates is that they appear to be decomposable into contributions from the

individual C^N and N^N ligands. We will refer to the ability of an individual ligand to promote

catalysis as the "strength" of that individual ligand and explore a number of ways to extract these

strengths from the measured rates. A particularly simple way to estimate the strength of a ligand

is to sum the observed rate over all complexes that include that ligand (Eqn. 1),

$$S^{margin}(cn) = \sum_{nn} Rate(cn,nn) \quad ; \qquad S^{margin}(nn) = \sum_{cn} Rate(cn,nn) \tag{1}$$

We refer to these as S^{margin} because these would be the margins of a two-dimensional data table

formed from Rate(cn,nn). A heat map of the reaction rates, with the C^N and N^N ligands sorted

by S^{margin} (Figure 7a), shows the tendency of Rate(cn,nn) to increase with S^{margin} of the individual ligands.

To help quantify this tendency, we considered two models that are based on the general idea of ligand strength but use alternative measures of this strength. The first is a *sum* model, in which the rate is written as a sum of the ligand strengths (Eqn. 2),

$$Rate(cn,nn) = S^{sum} (cn) + S^{sum} (nn) \tag{2}$$

The second model assumes the rate is a product of ligand strengths (Eqn. 3),

$$Rate(cn,nn) = S^{product} (cn) * S^{product} (nn) \tag{3}$$

For both models, a least squares procedure is used to fit the model parameters, S^{sum} or $S^{product}$, to the observed rates. Each model has 72 parameters, one each for the 48 C^N and 24 N^N ligands, which can be fit to the rates measured for the 1152 catalysts. Separating the data into train and test sets has little impact on the quality of the model predictions (see Supporting Information). Although both the *sum* (Figure 7b) and *product* (Figure 7c) model can account for a large proportion of the variance in the data, the *product* model performs better (r^2 of 0.87 for *product* model versus 0.74 for *sum* model).
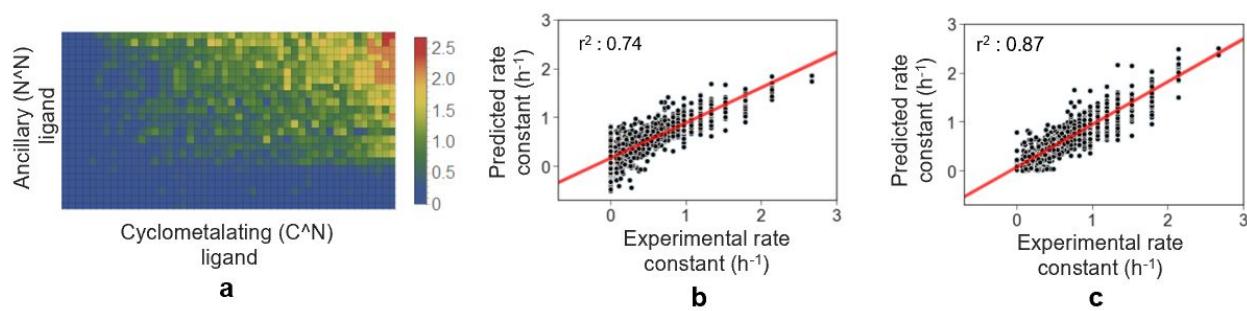

Figure 7. **a**. Heatmap of rate constants as a function of C^N and N^N ligands, with ligands sorted from poor to good performers, as measured by S^{margin}. The scatterplots show the predicted rate versus the experimental rate from the *sum* model (**b**) the *product* model (**c**).

18

The *product* model also gives more reasonable results for catalysts with low performance, with predicted rates for these complexes having a smaller variance than for the *sum* model and with all predicted rates remaining positive. This reflects the tendency, apparent in the heat map, for poorly-performing ligands to lead to poorly-performing catalysts, even when paired with a strong partner ligand. The variables, S^{margin}, S^{sum}, and $S^{product}$, provide quantitative measures of the strength of each ligand. The rankings of ligands, from poor to strong performers, obtained for S^{sum} are identical to those with S^{margin}, while slight reordering occurs with $S^{product}$ (see Supporting Information). Our use of the *sum* and *product* models is primarily intended to quantify the tendency of the rate to decompose into contributions from the individual ligands. However, it is interesting to note that the product model is what would be expected if the relevant chemical properties of the ligands were associated with energies or other properties that, in the relation for the rate constant, appear in an exponential.

The ability of these models to explain a large proportion of the variance in the experimental data validates that our measured rates are not simply results of random changes in indicator dye but are instead meaningful trends in catalysts' properties. It is also interesting to observe that properties of the ligands alone are able to establish meaningful correlations, as seen in other chemical fragment-based approaches employed in data-driven analysis of catalytic systems.[62-65] The above models are only able to make predictions for complexes containing already studied ligands. In ongoing work, we are using DFT-derived features to enable the prediction of photocatalyst activity exclusively from chemical structure.

Conventional Tests with Selected Photocatalysts

The HTSS identified several iridium(III) complexes with impressive reactivities compared to the most commonly used commercial photoredox catalysts. To further explore the results we selected four complexes to traditionally synthesize and fully characterize: **[Ir(CN40)$_2$(NN6)]$^+$**, **[Ir(CN35)$_2$(NN6)]$^+$**, **[Ir(CN35)$_2$(NN16)]$^+$** and the highly active photocatalyst **[Ir(CN63)$_2$(NN6)]$^+$** (see Figure 8 for structures). The optical, electrochemical and DFT calculated properties of the photocatalysts were compared to the most commonly used photoredox catalysts **[Ir(CN1)$_2$(NN6)]$^+$** and **[Ir(CN14)$_2$(NN6)]$^+$** ([Ir(ppy)$_2$(dtbbpy)]PF$_6$ and [Ir(dF(CF$_3$)ppy)$_2$(dtbbpy)]PF$_6$).
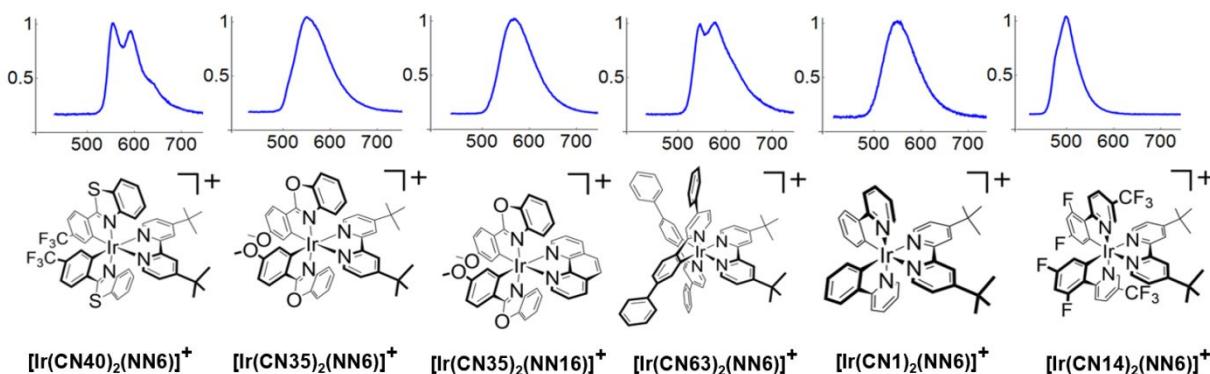
Figure 8. Normalized room temperature emission spectra of the six [Ir(C^N)$_2$(N^N)]$^+$ photocatalysts. The argon degassed samples (20 µM acetonitrile solutions) were excited at $\lambda = 365$ nm, and their luminescence spectrum was measured at room temperature.

Absorbance spectra were measured in acetonitrile and are analogous to other reported heteroleptic cationic iridium(III) complexes.[66] Below 300 nm all compounds exhibit intense ligand-centered (LC) transitions, while absorptions at longer wavelengths are assigned to metal-ligand-to-ligand charge transfer (MLLCT) transitions. Emission spectra revealed that **[Ir(CN35)$_2$(NN6)]$^+$** and **[Ir(CN35)$_2$(NN16)]$^+$** exhibited a broad structureless emission indicative of a predominately ^{3}MLLCT excited state.[67] The vibronic substructure observed in the other

synthesized complexes indicates the often observed mixing with an ^{3}LC excited state. This is also reflected in the longer lifetimes of these complexes, compared to the relatively short measured lifetime for the mostly ^{3}MLLCT excited state complex **[Ir(CN1)$_2$(NN6)]$^+$** (Table 1).

Table 1. Photophysical, electrochemical and density functional theory (DFT) calculated data of the selected iridium(III) complexes. Also, the HTSS rate constant values from the dehalogenation the bromopentafluorobenzene are included.

	[Ir(CN40)$_2$(NN6)]$^+$	[Ir(CN35)$_2$(NN6)]$^+$	[Ir(CN35)$_2$(NN16)]$^+$	[Ir(CN63)$_2$(NN6)]$^+$	[Ir(CN1)$_2$(NN6)]$^+$	[Ir(CN14)$_2$(NN6)]$^+$
Absorption						
λ_{abs}/ nm (ε/ x10^3 M^{-1} cm^{-1})	297(23.4), 311(23.5), 324(20.7), 410(4.6)	271(34.2), 297(30.9), 387(9.6)	271(46.7), 299(32.2), 374(13.5)	273(46.9), 295(53.0), 404(6.2)	257(35.2), 410(0.60)	260(55.0), 310(33.9), 380(6.2)
Emission						
λ_{em}/ nm	577	551	561	535	571	480
τ/ µs	2.2	1.8	1.6	2.1	0.6	2.3
Electrochemistry						
E^0(Ir^{4+}/Ir^{3+})/ V	1.69	1.3	1.48	1.24	1.21	1.69
E^0(Ir^{3+}/Ir^{2+})/ V	−1.37	−1.44	−1.28	−1.46, −1.90, −2.07	−1.51	−1.37, −1.68
DFT calculations						
HOMO/ eV	-5.19	-4.85	-5.16	-4.69	-4.85	-5.42
LUMO/ eV	-8.46	-7.75	-7.79	-7.44	-7.72	-8.9
HOMO-LUMO gap/ eV	3.27	2.9	2.63	2.75	2.87	3.48
HTSS rate constants/ h^{-1}	1.53	1.07	0.09	2.14	0.89	0.63

Electrochemical analysis showed varied behavior, from **[Ir(CN40)$_2$(NN6)]$^+$** with a strongly positive reversible oxidation potential, similar to the state-of-art **[Ir(CN14)$_2$(NN6)]$^+$** used in systems that proceed *via* an oxidative quenching mechanism to **[Ir(CN63)$_2$(NN6)]$^+$** with reversible and quasi-reversible reductions at -1.46, -1.90 and -2.07 V vs SCE (Figure 9). With only the six photocatalysts, no direct correlation between the luminescence maximum energy, redox potentials or calculated HOMO-LUMO gaps can be found, indicating that extensive photophysical and electrochemical data and DFT calculations are necessary to establish such correlations.
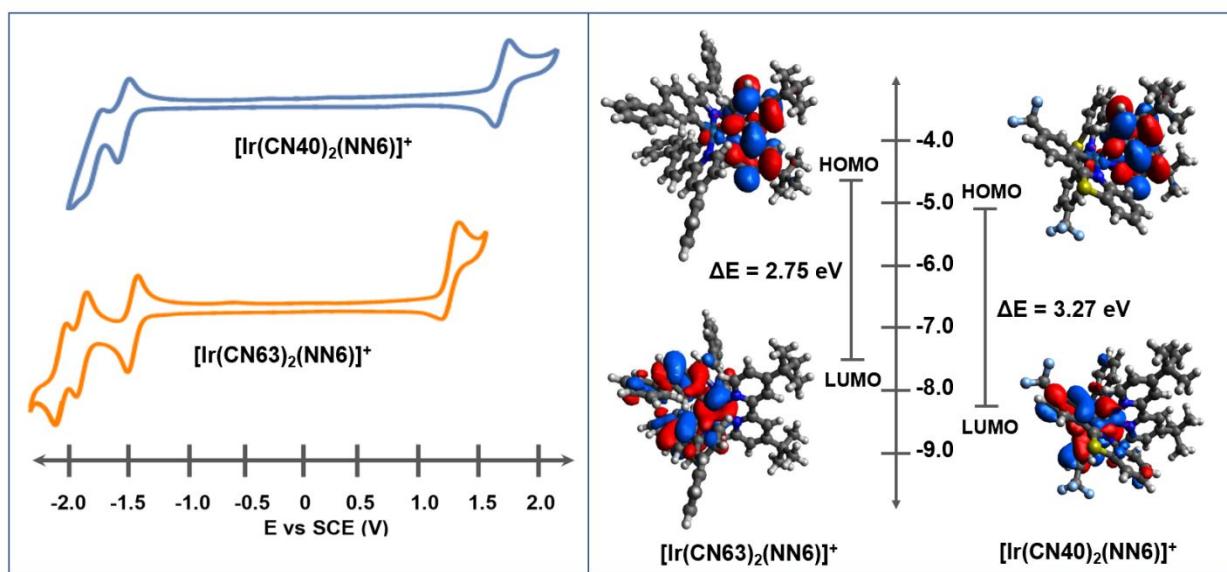
Figure 9. Comparison of the electrochemistry and DFT of two iridium(III) complexes; **[Ir(CN40)₂(NN6)]⁺** shows a strongly positive oxidation potential, while the second compound (**[Ir(CN63)₂(NN6)]⁺**) exhibit multiple reduction peaks. The DFT calculations document the widely different energy of the involved frontier orbitals which highlights that structure-activity are much more complex and, consequently, a HTSS approach is necessary until better correlations with calculated features allow the accurate prediction of reactivity from quantum mechanics.

Insight obtained from the developed rapid screening approach may assist the identification of photocatalysts that demonstrate thermodynamic and kinetic reaction control. Chemoselective dehalogenation of trisubstituted aryl halides is reported with organic dye photocatalysts[68] but the modular synthesis of metal complexes allows comparatively facile tuning of redox and photophysical properties. The variation in activity of the six synthesized complexes in the debromination of 1,2-dibromo-4,5-difluorobenzene was monitored by ^{19}F NMR (Figure 10).

| Photocatalyst	1 hr.		16 hr.	
	B (%)	C (%)	B (%)	C (%)
[Ir(CN40)$_2$NN6]$^+$	11	0	84	0
[Ir(CN35)$_2$NN6]$^+$	30	0	92	8
[Ir(CN35)$_2$NN16]$^+$	9	0	95	0
[Ir(CN63)$_2$NN6]$^+$	75	25	0	99
[Ir(CN1)$_2$NN6]$^+$	29	0	84	16
[Ir(CN14)$_2$NN6]$^+$	25	0	65	35
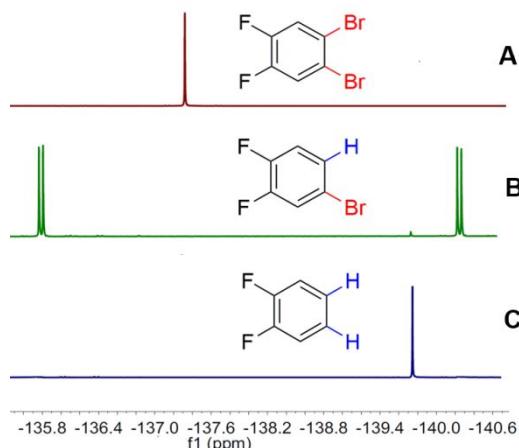
Figure 10. ^{19}F NMR analysis of the dehalogenation of 1,2-dibromo-4,5-difluorobenzene (**A**, singlet peak, δ -137.3 ppm), catalyzed by six different photocatalysts. The first dehalogenation product, 4-bromo-1,2-difluorobenzene (**B,** doublet, δ -135.8 and -140.4 ppm) and the fully debrominated product 1,2-difluorobenzene (**C,** singlet, δ -139.7 ppm) can be obtained exclusively and in almost quantitative yields by two different photocatalysts (species **B** by **[Ir(CN35)$_2$(NN16)]$^+$** and **C** by **[Ir(CN63)$_2$(NN6)]$^+$**) .

The three complexes containing either 2-phenylbenzothiazole or 2-phenylbenzoxazole cyclometalating ligands all produced the singly debrominated product in high yield after 16 hours irradiation, while **[Ir(CN63)$_2$(NN6)]$^+$** quantitatively produced 1,2-difluorobenzene. In comparison, both commercial photoredox catalysts (**[Ir(CN1)$_2$(NN6)]$^+$** and **[Ir(CN14)$_2$(NN6)]$^+$**) yielded a mixture of products. This promising result suggests similar chemoselectivity in C–C bond forming reactions, comparable to that observed with some organic dyes can be achieved.[69-70] Zeitler's work with the organic dyes highlights this importance of tuning the photocatalysts from highly oxidizing to highly reducing potentials to achieve targeted catalysis. We believe the heteroleptic Ir(III) photocatalysts offer a much more accessible platform for synthetically tuning their activity and selectivity compared to organic dye molecules. Also, the very efficient and fast

23

chromophore **[Ir(CN63)$_2$(NN6)]$^+$** is comparatively easy to synthesize and does not contain any expensive and environmentally problematic fluorine substitutions.

CONCLUSION

The presented work allowed the development of an indicator dye-based methodology for the online monitoring of the catalytic performance of 1152 *in-situ* synthesized cationic iridium(III) complexes in photoredox processes. The utility of this technique was demonstrated through rapid screening of the C^N and N^N ligands parameter space to pinpoint champion catalysts for the dehalogenation of aryl bromide. In addition to accelerating chemical discovery, this colorimetric approach is a significant step towards providing large sets of standardized experimental data that, in future work, can be combined with computationally derived features to build towards highly predictive machine learning models. Results obtained from this data-driven inquiry were confirmed via traditional synthesis and characterization techniques. The reactivity of some newly synthesized photocataysts exceeded those of the most well-studied and commercially-used cationic Ir(III) complexes by a factor of 3-4. It was also possible to tailor the discovered catalysts for chemoselectivity.

ASSOCIATED CONTENT

Supporting Information

All supporting figures and tables, Wolfram Mathematica code for image analysis and data processing, Python code for photoreactor control and data modeling, as well as a description of data modeling with train-test splits, are presented in a PDF document. Also attached is the csv file of the 1152 rate constants and the two videos of real-time reaction progress mentioned in the main text. This material is all available free of charge at http://pubs.acs.org.

AUTHOR INFORMATION

Corresponding Author

*bern@cmu.edu

Notes

The authors declare no competing financial interest.

ACKNOWLEDGEMENTS

REFERENCES

1. Rossi, R. A.; Pierini, A. B.; Peñéñory, A. B. Nucleophilic Substitution Reactions by Electron Transfer. *Chem. Rev.* **2003,** *103*, 71-167.

2. Reckenthäler, M.; Griesbeck, A. G. Photoredox Catalysis for Organic Syntheses. *Adv. Synth. Catal.* **2013,** *355*, 2727-2744.

3. Wang, C.-S.; Dixneuf, P. H.; Soulé, J.-F. Photoredox Catalysis for Building C–C Bonds from C(sp^2)–H Bonds. *Chem. Rev.* **2018,** *118*, 7532-7585.

4. Prier, C. K.; Rankic, D. A.; MacMillan, D. W. C. Visible Light Photoredox Catalysis with Transition Metal Complexes: Applications in Organic Synthesis. *Chem. Rev.* **2013,** *113*, 5322-5363.

5. Nicholls, T. P.; Leonori, D.; Bissember, A. C. Applications of Visible Light Photoredox Catalysis to the Synthesis of Natural Products and Related Compounds. *Nat. Prod. Rep.* **2016,** *33*, 1248-1254.

6. Douglas, J. J.; Sevrin, M. J.; Stephenson, C. R. J. Visible Light Photocatalysis: Applications and New Disconnections in the Synthesis of Pharmaceutical Agents. *Org. Process Res. Dev.* **2016,** *20*, 1134-1147.

7. DiRocco, D. A.; Dykstra, K.; Krska, S.; Vachal, P.; Conway, D. V.; Tudge, M. Late-Stage Functionalization of Biologically Active Heterocycles Through Photoredox Catalysis. *Angew. Chem. Int. Ed.* **2014,** *53*, 4802-4806.

8. Romero, N. A.; Nicewicz, D. A. Organic Photoredox Catalysis. *Chem. Rev.* **2016,** *116*, 10075-10166.

9. Larsen, C. B.; Wenger, O. S. Photoredox Catalysis with Metal Complexes Made from Earth-Abundant Elements. *Chem. Eur. J.* **2018,** *24*, 2039-2058.

10. Goldsmith, J. I.; Hudson, W. R.; Lowry, M. S.; Anderson, T. H.; Bernhard, S. Discovery and High-Throughput Screening of Heteroleptic Iridium Complexes for Photoinduced Hydrogen Production. *J. Am. Chem. Soc.* **2005,** *127*, 7502-7510.

11. Yuan, Y.-J.; Yu, Z.-T.; Chen, D.-Q.; Zou, Z.-G. Metal-Complex Chromophores for Solar Hydrogen Generation. *Chem. Soc. Rev.* **2017,** *46*, 603-631.

12. Mills, I. N.; Porras, J. A.; Bernhard, S. Judicious Design of Cationic, Cyclometalated Ir(III) Complexes for Photochemical Energy Conversion and Optoelectronics. *Acc. Chem. Res.* **2018,** *51*, 352-364.

13. Lo, K. K.-W.; Louie, M.-W.; Zhang, K. Y. Design of Luminescent Iridium(III) and Rhenium(I) Polypyridine Complexes as in Vitro and in Vivo Ion, Molecular and Biological Probes. *Coord. Chem. Rev.* **2010,** *254*, 2603-2622.

14. Caporale, C.; Massi, M. Cyclometalated Iridium(III) Complexes for Life Science. *Coord. Chem. Rev.* **2018,** *363*, 71-91.

15. Connell, T. U.; Donnelly, P. S. Labelling Proteins and Peptides with Phosphorescent d^6 Transition Metal Complexes. *Coord. Chem. Rev.* **2018,** *375*, 267-284.

16. Flamigni, L.; Barbieri, A.; Sabatini, C.; Ventura, B.; Barigelletti, F. Photochemistry and Photophysics of Coordination Compounds: Iridium. In *Photochemistry and Photophysics of Coordination Compounds II*, Balzani, V.; Campagna, S. Eds. Springer Berlin Heidelberg: Berlin, Heidelberg, 2007; pp 143-203.

17. Choy, W. C. H.; Chan, W. K.; Yuan, Y. Recent Advances in Transition Metal Complexes and Light-Management Engineering in Organic Optoelectronic Devices. *Adv. Mater.* **2014,** *26*, 5368-5399.

18. Kagalwala, H. N.; Chirdon, D. N.; Bernhard, S. Solar Fuel Generation. In *Iridium(III) in Optoelectronic and Photonics Applications*, 2017; pp 583-615.

19. Reddington, E.; Sapienza, A.; Gurau, B.; Viswanathan, R.; Sarangapani, S.; Smotkin, E. S.; Mallouk, T. E. Combinatorial Electrochemistry: A Highly Parallel, Optical Screening Method for Discovery of Better Electrocatalysts. *Science* **1998,** *280*, 1735-1737.

20. Jun, Y. J.; Park, S. H.; Woo, S. I. Combinatorial High-Throughput Optical Screening of High Performance Pd Alloy Cathode for Hybrid Li − Air Battery. *ACS Comb. Sci.* **2014,** *16*, 670-677.

21.   Park, S. H.; Choi, C. H.; Koh, J. K.; Pak, C.; Jin, S.-a.; Woo, S. I. Combinatorial High-Throughput Screening for Highly Active Pd − Ir − Ce Based Ternary Catalysts in Electrochemical Oxygen Reduction Reaction. *ACS Comb. Sci.* **2013,** *15*, 572-579.

22.   Baud, D.; Ladkau, N.; Moody, T. S.; Ward, J. M.; Hailes, H. C. A Rapid, Sensitive Colorimetric Assay for High-Throughput Screening of Transaminases in Liquid or Solid-Phase. *Chem. Commun.* **2015,** *51*, 17225-17228.

23.   Shaughnessy, K. H.; Kim, P.; Hartwig, J. F. A Fluorescence-Based Assay for High-Throughput Screening of Coupling Reactions. Application to Heck Chemistry. *J. Am. Chem. Soc.* **1999,** *121*, 2123-2132.

24.   Crabtree, R. H. Combinatorial and Rapid Screening Approaches to Homogeneous Catalyst Discovery and Optimization. *Chem. Commun.* **1999**, 1611-1616.

25.   Copeland, G. T.; Miller, S. J. A Chemosensor-Based Approach to Catalyst Discovery in Solution and on Solid Support. *J. Am. Chem. Soc.* **1999,** *121*, 4306-4307.

26.   Shah, R.; Pratt, D. A. Determination of Key Hydrocarbon Autoxidation Products by Fluorescence. *J. Org. Chem.* **2016,** *81*, 6649-6656.

27.   Boussie, T. R.; Diamond, G. M.; Goh, C.; Hall, K. A.; Lapointe, A. M.; Leclerc, M.; Lund, C.; Murphy, V.; Shoemaker, J. A. W.; Tracht, U.; Turner, H.; Zhang, J.; Uno, T.; Rosen, R. K.; Stevens, J. C. A Fully Integrated High-Throughput Screening Methodology for the Discovery of New Polyolefin Catalysts: Discovery of a New Class of High Temperature Single-Site Group (IV) Copolymerization Catalysts. *J. Am. Chem. Soc.* **2003,** *125*, 4306-4317.

28.   Mitrovic, S.; Soedarmadji, E.; Newhouse, P. F.; Suram, S. K.; Haber, J. A.; Jin, J.; Gregoire, J. M. Colorimetric Screening for High-Throughput Discovery of Light Absorbers. *ACS Comb. Sci.* **2015,** *17*, 176-181.

29.   Curtin, P. N.; Tinker, L. L.; Burgess, C. M.; Cline, E. D.; Bernhard, S. Structure−Activity Correlations Among Iridium(III) Photosensitizers in a Robust Water-Reducing System. *Inorg. Chem.* **2009,** *48*, 10498-10506.

30.   Lee, J.-H.; Cheglakov, Z.; Yi, J.; Cronin, T. M.; Gibson, K. J.; Tian, B.; Weizmann, Y. Plasmonic Photothermal Gold Bipyramid Nanoreactors for Ultrafast Real-Time Bioassays. *J. Am. Chem. Soc.* **2017,** *139*, 8054-8057.

31.   Gerry, C. J.; Hua, B. K.; Wawer, M. J.; Knowles, J. P.; Nelson Jr, S. D.; Verho, O.; Dandapani, S.; Wagner, B. K.; Clemons, P. A.; Booker-Milburn, K. I.; Boskovic, Z. V.; Schreiber, S. L. Real-Time Biological Annotation of Synthetic Compounds. *J. Am. Chem. Soc.* **2016,** *138*, 8920-8927.

32.   Lopato, E. M.; Eikey, E. A.; Simon, Z. C.; Back, S.; Tran, K.; Lewis, J.; Kowalewski, J. F.; Yazdi, S.; Kitchin, J. R.; Ulissi, Z. W.; Millstone, J. E.; Bernhard, S. Parallelized Screening of Characterized and DFT-Modelled Bimetallic Colloidal Co-Catalysts for Photocatalytic Hydrogen Evolution. *ACS Catal.* **2020**, 10, 4244-4252.

33.   Hey, T.; Tansley, S.; Tolle, K. The Fourth Paradigm Data-Intensive Scientific Discovery. Microsoft Research: Redmond, WA, 2009.

34.   Bonk, B. M.; Weis, J. W.; Tidor, B. Machine Learning Identifies Chemical Characteristics That Promote Enzyme Catalysis. *J. Am. Chem. Soc.* **2019,** *141*, 4108-4118.

35.   Bai, Y.; Wilbraham, L.; Slater, B. J.; Zwijnenburg, M. A.; Sprick, R. S.; Cooper, A. I. Accelerated Discovery of Organic Polymer Photocatalysts for Hydrogen Evolution from Water through the Integration of Experiment and Theory. *J. Am. Chem. Soc.* **2019,** *141*, 9063-9071.

36.   Palkovits, R.; Palkovits, S. Using Artificial Intelligence to Forecast Water Oxidation Catalysts. *ACS Catal.* **2019,** *9*, 8383-8387.

37.   Masood, H.; Ying Toe, C.; Yang Teoh, W.; Sethu, V.; Amal, R. Machine Learning for Accelerated Discovery of Solar Photocatalysts. *ACS Catal.* **2019,** *9*, 11774−11787.

38.   Mills, I. N.; Kagalwala, H. N.; Bernhard, S. Cyano-Decorated Ligands: A Powerful Alternative to Fluorination for Tuning the Photochemical Properties of Cyclometalated Ir(III) Complexes. *Dalton Trans.* **2016,** *45*, 10411-10419.

39.   Lowry, M. S.; Hudson, W. R.; Pascal, R. A.; Bernhard, S. Accelerated Luminophore Discovery through Combinatorial Synthesis. *J. Am. Chem. Soc.* **2004,** *126*, 14129-14135.

40.   Ghodbane, A.; D'Altério, S.; Saffon, N.; McClenaghan, N. D.; Scarpantonio, L.; Jolinat, P.; Fery-Forgues, S. Facile Access to Highly Fluorescent Nanofibers and Microcrystals via Reprecipitation of 2-Phenyl-benzoxazole Derivatives. *Langmuir* **2012,** *28*, 855-863.

41.   Banerjee, M.; Chatterjee, A.; Kumar, V.; Bhutia, Z. T.; Khandare, D. G.; Majik, M. S.; Roy, B. G. A Simple and Efficient Mechanochemical Route for the Synthesis of 2-Aryl Benzothiazoles and Substituted Benzimidazoles. *RSC Adv.* **2014,** *4*, 39606-39611.

42.   Weekes, A. A.; Bagley, M. C.; Westwell, A. D. An Efficient Synthetic Route to Biologically Relevant 2-Phenylbenzothiazoles Substituted on the Benzothiazole Ring. *Tetrahedron* **2011,** *67*, 7743-7747.

43.   Pedregosa, F.; Varoquaux, G.; Gramfort, A.; Michel, V.; Thirion, B.; Grisel, O.; Blondel, M.; Prettenhofer, P.; Weiss, R.; Dubourg, V.; Vanderplas, J.; Passo, A.; Cournapeau, D.; Brucher, M.; Perrot, M.; Duchesnay, É. Scikit-Learn: Machine Learning in Python. *J. Mach. Learn. Res.* **2011,** *12*, 2825−2830.

44.   Connelly, N. G.; Geiger, W. E. Chemical Redox Agents for Organometallic Chemistry. *Chem. Rev.* **1996,** *96*, 877-910.

45.   Devery, J. J.; Nguyen, J. D.; Dai, C.; Stephenson, C. R. J. Light-Mediated Reductive Debromination of Unactivated Alkyl and Aryl Bromides. *ACS Catal.* **2016,** *6*, 5962-5967.

46.   Pal, A.; Ghosh, I.; Sapra, S.; König, B. Quantum Dots in Visible-Light Photoredox Catalysis: Reductive Dehalogenations and C-H Arylation Reactions Using Aryl Bromides. *Chem. Mater.* **2017,** *29*, 5225-5231.

47.   Shon, J.-H.; Sittel, S.; Teets, T. S. Synthesis and Characterization of Strong Cyclometalated Iridium Photoreductants for Application in Photocatalytic Aryl Bromide Hydrodebromination. *ACS Catal.* **2019,** *9*, 8646-8658.

48.   Ghosh, I.; Ghosh, T.; Bardagi, J. I.; König, B. Reduction of Aryl Halides by Consecutive Visible Light-Induced Electron Transfer Processes. *Science* **2014,** *346*, 725-728.

49.   Poznik, M.; König, B. Fast Colorimetric Screening for Visible Light Photocatalytic Oxidation and Reduction Reactions. *React. Chem. Eng.* **2016,** *1*, 494-500.

50.   Mina, M. V.; Puzyk, I. P.; Puzyk, M. V. The Effect of Acids on Fluorescence of Coumarin-6 in Organic Solvents. *Opt. Spectrosc.* **2013,** *114*, 244-246.

51.   Vasylevska, A. S.; Karasyov, A. A.; Borisov, S. M.; Krause, C. Novel Coumarin-Based Fluorescent pH Indicators, Probes and Membranes Covering a Broad pH Range. *Anal. and Bioanal. Chem.* **2007,** *387*, 2131-2141.

52.   Mason, M. D.; Ray, K.; Pohlers, G.; Cameron, J. F.; Grober, R. D. Probing the Local pH of Polymer Photoresist Films Using a Two-Color Single Molecule Nanoprobe. *J. Phys. Chem. B* **2003,** *107*, 14219-14224.

53.   Meyer, A. U.; Slanina, T.; Yao, C.-J.; König, B. Metal-Free Perfluoroarylation by Visible Light Photoredox Catalysis. *ACS Catal.* **2016,** *6*, 369-375.

54.   Garces, F. O.; King, K. A.; Watts, R. J. Synthesis, Structure, Electrochemistry, and Photophysics of Methyl-Substituted Phenylpyridine Ortho-Metalated Iridium(III) Complexes. *Inorg. Chem.* **1988,** *27*, 3464-3471.

55.   Tinker, L. L.; McDaniel, N. D.; Curtin, P. N.; Smith, C. K.; Ireland, M. J.; Bernhard, S. Visible Light Induced Catalytic Water Reduction without an Electron Relay. *Chem. Eur. J.* **2007,** *13*, 8726-8732.

56.   Zhao, Q.; Liu, S.; Shi, M.; Wang, C.; Yu, M.; Li, L.; Li, F.; Yi, T.; Huang, C. Series of New Cationic Iridium(III) Complexes with Tunable Emission Wavelength and Excited State Properties: Structures, Theoretical Calculations, and Photophysical and Electrochemical Properties. *Inorg. Chem.* **2006,** *45*, 6152-6160.

57.   Zeng, X.; Tavasli, M.; Perepichka, I. F.; Batsanov, A. S.; Bryce, M. R.; Chiang, C. J.; Rothe, C.; Monkman, A. P. Cationic Bis-Cyclometallated Iridium(III) Phenanthroline Complexes with Pendant

Fluorenyl Substituents: Synthesis, Redox, Photophysical Properties and Light-Emitting Cells. *Chem. Eur. J.* **2008,** *14*, 933-943.

58.   Lamansky, S.; Djurovich, P.; Murphy, D.; Abdel-Razzaq, F.; Lee, H. E.; Adachi, C.; Burrows, P. E.; Forrest, S. R.; Thompson, M. E. Highly Phosphorescent Bis-Cyclometalated Iridium Complexes: Synthesis, Photophysical Characterization, and Use in Organic Light Emitting Diodes. *J. Am. Chem. Soc.* **2001,** *123*, 4304-4312.

59.   Marcus, R. A. Electron Transfer Reactions in Chemistry: Theory and Experiment (Nobel Lecture). *Angew. Chem. Int. Ed.* **1993,** *32*, 1111-1121.

60.   Hasan, K.; Bansal, A. K.; Samuel, I. D. W.; Roldán-Carmona, C.; Bolink, H. J.; Zysman-Colman, E. Tuning the Emission of Cationic Iridium(III) Complexes Towards the Red Through Methoxy Substitution of the Cyclometalating Ligand. *Sci. Rep.* **2015,** *5*, 12325.

61.   Peloquin, A. J.; Smith, M. B.; Balaich, G. J.; Iacono, S. T. Crystal Structure of Chlorido(dimethyl sulfoxide-κS)bis[4-(pyridin-2-yl)benzaldehyde-κ^{3}C^2,N]iridium(III) Acetonitrile Monosolvate. *Acta Crystallogr., Sect. E, Cryst. Commun.* **2017,** *73*, 1279-1281.

62.   Janet, J. P.; Liu, F.; Nandy, A.; Duan, C.; Yang, T.; Lin, S.; Kulik, H. J. Designing in the Face of Uncertainty: Exploiting Electronic Structure and Machine Learning Models for Discovery in Inorganic Chemistry. *Inorg. Chem.* **2019,** *58*, 10592-10606.

63.   Cruz, V. L.; Martinez, S.; Ramos, J.; Martinez-Salazar, J. 3D-QSAR as a Tool for Understanding and Improving Single-Site Polymerization Catalysts. A Review. *Organometallics* **2014,** *33*, 2944-2959.

64.   Tortorella, S.; Marotta, G.; Cruciani, G.; De Angelis, F. Quantitative Structure–Property Relationship Modeling of Ruthenium Sensitizers for Solar Cells Applications: Novel Tools for Designing Promising Candidates. *RSC Adv.* **2015,** *5*, 23865-23873.

65.   Fey, N.; Orpen, A. G.; Harvey, J. N. Building Ligand Knowledge Bases for Organometallic Chemistry: Computational Description of Phosphorus(III)-Donor Ligands and the Metal–Phosphorus Bond. *Coord. Chem. Rev.* **2009,** *253*, 704-722.

66.   Deaton, J. C.; Castellano, F. N. Archetypal Iridium(III) Compounds for Optoelectronic and Photonic Applications. In *Iridium(III) in Optoelectronic and Photonics Applications*, 2017; pp 1-69.

67.   Li, Y.; Dandu, N.; Liu, R.; Hu, L.; Kilina, S.; Sun, W. Nonlinear Absorbing Cationic Iridium(III) Complexes Bearing Benzothiazolylfluorene Motif on the Bipyridine (N^N) Ligand: Synthesis, Photophysics and Reverse Saturable Absorption. *ACS Appl. Mater. Interfaces* **2013,** *5*, 6556-6570.

68.   Poelma, S. O.; Burnett, G. L.; Discekici, E. H.; Mattson, K. M.; Treat, N. J.; Luo, Y.; Hudson, Z. M.; Shankel, S. L.; Clark, P. G.; Kramer, J. W.; Hawker, C. J.; Read de Alaniz, J. Chemoselective Radical Dehalogenation and C–C Bond Formation on Aryl Halide Substrates Using Organic Photoredox Catalysts. *J. Org. Chem.* **2016,** *81*, 7155-7160.

69.   Ghosh, I.; König, B. Chromoselective Photocatalysis: Controlled Bond Activation through Light-Color Regulation of Redox Potentials. *Angew. Chem. Int. Ed.* **2016,** *55*, 7676-7679.

70.   Speckmeier, E.; Fischer, T. G.; Zeitler, K. A Toolbox Approach To Construct Broadly Applicable Metal-Free Catalysts for Photoredox Chemistry: Deliberate Tuning of Redox Potentials and Importance of Halogens in Donor–Acceptor Cyanoarenes. *J. Am. Chem. Soc.* **2018,** *140*, 15353-15365.

For Table of Contents Use: